Accepted Manuscript

Title: Synergistic Effect of Core-Shell Heterogeneous V$_2$O$_5$@MV$_6$O$_{15}$ (M = Na, K) Nanoparticles for Enhanced Lithium Storage Performance

Authors: Meng Huang, Caiyi Zhang, Chunhua Han, Xiaoming Xu, Xiong Liu, Kang Han, Qi Li, Liqiang Mai

Please cite this article as: Meng Huang, Caiyi Zhang, Chunhua Han, Xiaoming Xu, Xiong Liu, Kang Han, Qi Li, Liqiang Mai, Synergistic Effect of Core-Shell Heterogeneous V2O5@MV6O15 (M=Na, K) Nanoparticles for Enhanced Lithium Storage Performance, Electrochimica Actahttp://dx.doi.org/10.1016/j.electacta.2017.09.077

Synergistic Effect of Core-Shell Heterogeneous V_2O_5@MV_6O_{15} (M=Na, K) Nanoparticles for Enhanced Lithium Storage Performance

Meng Huang,[†,‡] Caiyi Zhang,[†,‡] Chunhua Han,*[,‡] Xiaoming Xu,[‡] Xiong Liu,[‡] Kang Han,[‡] Qi Li,[‡] Liqiang Mai*[,‡,§]

[‡] State Key Laboratory of Advanced Technology for Materials Synthesis and Processing, International School of Materials Science and Engineering, Wuhan University of Technology, Wuhan 430070, China

[§] Department of Chemistry, University of California, Berkeley, California 94720, United States
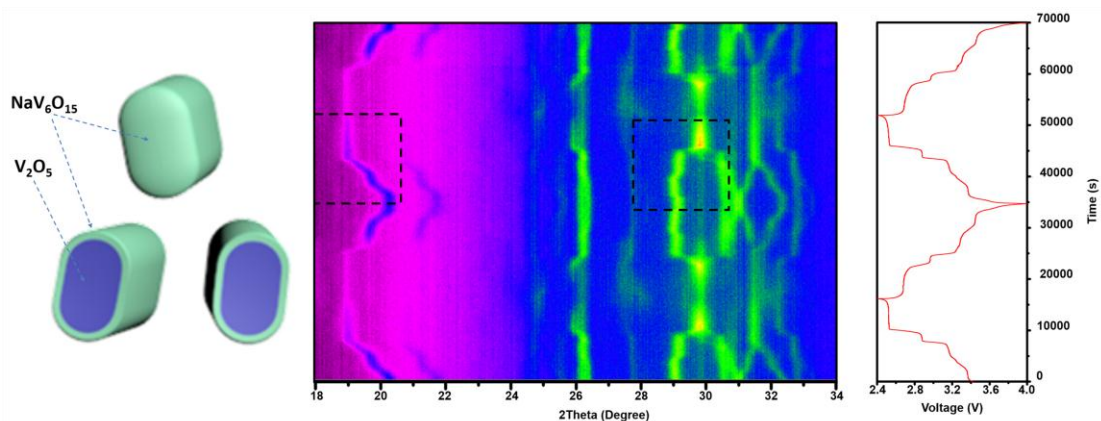
* Correspondence authors.

E-mail addresses: mlq518@whut.edu.cn (L. Mai)

hch5927@whut.edu.cn (C. Han)

[†] The authors contributed equally to this manuscript.

Graphical abstract

Highlights

- V_2O_5@MV_6O_{15} (M=Na, K) NPs are successfully constructed through a facile "semi-solid" synthetic method.
- The V_2O_5@MV_6O_{15} NPs show much enhanced electrochemical performance as compared to V_2O_5.
- The enhanced performances are attributed to the synergistic effects from the outer MV_6O_{15} layers.
- The synergistic effects are confirmed by the *in-situ* XRD testing results.

Abstract:

Synergistic effects of heterostructures can improve electrochemical properties of electrode materials. Herein, core-shell heterogeneous structures of V_2O_5@MV_6O_{15} (M=Na, K) nanoparticles were designed and successfully synthesized through a facile "semi-solid" method. V_2O_5@NaV_6O_{15} nanoparticles showed a high discharge capacity of 140 mAh g^{-1} at 200 mA g^{-1} which retained 94.9% after 200 cycles, higher than those of V_2O_5 nanoparticles (116.1 mAh g^{-1} and 58%). Moreover, through an advanced *in-situ* XRD technology, the synergistic effect of buffering and smoothing Li^+ diffusion from MV_6O_{15} outer layer was revealed. This facile strategy could be widely applied to improve the electrochemical performances of other electrode materials.

1. Introduction

Energy storage systems based on lithium-ion batteries (LIBs) are one of the most

suitable and promising candidates for portable electronic devices.[1] However, the energy/power density, rate performance and energy efficiency of the current commercial LIBs still need to be improved to meet the growing demand of energy storage systems in the applications of electric vehicles (EVs), hybrid electric vehicles (HEVs) and etc.[2-4] For example, most of the promising cathode materials suffer from poor structural stability, low electronic/ionic conductivity and inert electrochemical kinetics, such as sulfur, NMC materials, transition metal fluorides and vanadium pentoxide (V_2O_5),[5-9] which result in low rate performance and energy efficiency, as well as limited cycling life in LIBs. Therefore, development of high-performance electrodes without above drawbacks through facile strategies such as complex structural design, nanotechnology and composite materials is hotspot and frontier in the energy storage field.[6-11]

Recently, constructing heterostructures which was widely studied in energy storage systems has been demonstrated as an effective strategy to enhance the electrochemical properties for cathode materials in both LIBs and sodium-ion batteries (SIBs).[12-15] Lee et al. constructed a layered P2/O3 intergrowth cathode for SIBs, which was interlocked from the layer shifting. The beneficial synergistic effect from the intergrowth structure promoting the smooth diffusion of Na^+ under a high rate testing was revealed by an *in-situ* synchrotron X-ray diffraction (XRD) study.[13] Wu et al. reported a $Li(Ni_xMn_yCo_z)O_2@LiFePO_4$ core-shell nanostructure with an atomic interdiffusion at the interface and an array of interconnected aligned Li^+ tunnels, which showed a high reversible capacity when used as a cathode in LIBs.[14] V_2O_5, a typical layered transition metal oxide, has attracted much attention for decades on account of its relatively high theoretical capacity, abundant resources and low cost, but it also suffers from the aforementioned problems of poor cycling stability in LIBs.[8-11] By contrast, MV_6O_{15} (M=Na, K) vanadates with "pillar-like" ions between the V-O interlayers and higher electronic conductivity show a more stable crystal structure and satisfactory cycling performance, and provide a faster Li^+ diffusion path, but deliver low capacity (Figure S1) in LIBs.[18-20, 29] Therefore, to

combine the merits from heterostructures and MV_6O_{15}, well designing of core-shell heterogeneous $V_2O_5@MV_6O_{15}$ nanoparticles (NPs) as cathode materials is expected to be able to enhance the electrochemical performances via a biphase synergistic effect.

Herein, utilizing a simple "semi-solid" method based on highly concentrated solution, we designed and constructed core-shell heterogeneous structures of $V_2O_5@NaV_6O_{15}$ and $V_2O_5@KV_6O_{15}$ NPs. When tested as cathodes in LIBs, both the core-shell heterogeneous structured NPs exhibit higher specific capacity, longer lifespan, as well as better rate capability compared to bare V_2O_5 NPs. Moreover, *in-situ* XRD tests were conducted and a synergistic effect (i.e. buffering and smoothing Li^+ diffusion) of the MV_6O_{15} outer layer was revealed, which accounts for the excellent lithium storage performance.

2. Experimental

2.1 Material:

Vanadium pentoxide (V_2O_5, AR, Xiya reagent Corporation, China), oxalic acid dihydrate ($C_2H_2O_4 \cdot 2H_2O$, AR, Sinopharm Group Chemical Reagent Co., Ltd., China), potassium citrate tribasic monohydtrate ($K_3C_6H_5O_7 \cdot H_2O$, AR, Sinopharm Group Chemical Reagent Co., Ltd., China), trisodium citrate dihydrate ($C_6H_5Na_3O_7 \cdot 2H_2O$, GR, Sinopharm Group Chemical Reagent Co., Ltd., China) and sodium alginate (($C_6H_7NaO_6)_n$, CP, Sinopharm Group Chemical Reagent Co., Ltd., China) were purchased and used without any purification.

2.2 Synthesis of $V_2O_5@NaV_6O_{15}$ and pure NaV_6O_{15} NPs

The VO_2 nanorod precursors were firstly synthesized according to a former published paper.[36] In a typical synthesis process: V_2O_5 (4 mmol) and $H_2C_2O_4 \cdot 2H_2O$ (8 mmol) were added into 80 mL of H_2O and stirred for 30 min at ambient temperature. Then the solution was transferred into a 100 mL Teflon autoclave and kept at 180 °C for 24 h. After cooling to room temperature, VO_2 nanorods were

successfully obtained by washing mildly with deionized water and pure alcohol several times and drying at 70 °C in air for 24 h. Then 3 mmol VO_2 nanorods and 0.05 mmol trisodium citrate dehydrate were mixed in 0.5 mL 0.2 wt% sodium alginate water solution in a mortar, and the mixture was grinded till dry powder was left. Next the dry powder was calcined in a muffle furnace firstly at a low temperature of 350 °C for 3 h, and then a high temperature of 450 °C for 2 h with the heating rate of 2 °C/min. The final product $V_2O_5@NaV_6O_{15}$ NPs were obtained after cooling down to ambient temperature. We can also adjust the composition ratio of $V_2O_5@NaV_6O_{15}$ by changing the amount of trisodium citrate dehydrate. Pure NaV_6O_{15} NPs were synthesized with the same procedure only by changing the amount of trisodium citrate dihydrate to 0.167 mmol and extending the calcining time at high temperature to 4 h.

2.3 Synthesis of $V_2O_5@KV_6O_{15}$ and pure KV_6O_{15} NPs

Like the synthesis of $V_2O_5@NaV_6O_{15}$ NPs. 3 mmol VO_2 nanorods and 0.05 mmol potassium citrate tribasic monohydtrate were mixed in 0.5 mL 0.2 wt% sodium alginate water solution in a mortar and the mixture was grinded till dry powder was left. Next the dry powder was calcined in a muffle furnace firstly at a low temperature of 350 °C for 3 h, and then a high temperature of 450 °C for 2 h with the heating rate of 2 °C/min. The final product $V_2O_5@KV_6O_{15}$ NPs were obtained after cooling down to ambient temperature. We can also adjust the composition ratio of $V_2O_5@NaV_6O_{15}$ by changing the amount of potassium citrate tribasic monohydtrate. Pure KV_6O_{15} NPs were synthesized with the same procedure only by changing the amount of potassium citrate tribasic monohydtrate to 0.167 mmol and extending the calcining time at high temperature to 4 h.

2.4 Synthesis of V_2O_5 NPs

V_2O_5 NPs were synthesized by grinding the VO_2 nanorods without any salt and solution that were added in the synthesis process of $V_2O_5@KV_6O_{15}$ NPs. Then the obtained powder was calcined with the same heat treatment process.

2.5 Material characterizations

The phase analysis of the final products was conducted over a 2θ range of 10º-80º at ambient temperature by utilizing a Bruker D8 Discover X-ray diffractometer with a Cu-Kα radiation source; for *in-situ* X-ray diffraction (XRD) measurements, the positive electrodes were covered by an X-ray-transparent beryllium window and the signals were received by the planar detector in a still mode during the testing process. The positive electrodes were fresh and each pattern took 2 min to acquire, during the first two original cycles of galvanostatic discharge/charge at the current density of 40 mA g^{-1}. Scanning electron microscope (SEM) images and energy-dispersive X-ray spectra (EDS) were collected by using a JEOL-7100 F SEM and an Oxford IE250 system, respectively. Transmission electron microscope (TEM) images were collected by using a Titan G2 60-300 with image corrector.

Electrochemical measurements

Type 2016 coin cells were assembled in a glovebox filled with pure argon gas. The positive electrodes were composed of 60 wt% $V_2O_5@NaV_6O_{15}$ NPs, $V_2O_5@KV_6O_{15}$ NPs or V_2O_5, 30 wt% acetylene black and 10 wt% polyvinylidene fluoride binders, which were coated on an aluminum foil. The mass loading of active materials is controlled at 1.3-1.5 mg cm^{-2}. Metallic Li foils were used as anode materials and a solution of $LiPF_6$ (1 M) in EC/DMC/EMC (1:1:1 vol/vol/vol) was used as electrolyte. Galvanostatic discharge/charge measurements were conducted in a multichannel battery testing system (LAND CT2001A). Cyclic voltammograms (CV) and electrochemical impedance spectra (EIS) were obtained utilizing an Autolab potentiostat/galvanostat. The EIS was conducted at initial open circuit potential (~3.4 V for $V_2O_5@MV_6O_{15}$ and V_2O_5 samples, and ~3.63 V for MV_6O_{15} samples) with the amplitude of AC signal of 0.01 V and frequency range between 0.01-100000 Hz.

3 Results and discussion

3.1 Morphologies and structures of as-prepared materials

The synthetic process of $V_2O_5@MV_6O_{15}$ NPs is shown in Figure 1a. In the hand milling process, the outer layer of the smooth-surfaced (Figure 1b) and pure-phased

(Figure S2) VO_2 nanorods which are 100-200 nm in width and 0.5-2.0 μm in length, reacts with MOH (M=Na, K) derived from the hydrolyzation of trisodium citrate dihydrate or potassium citrate tribasic monohydtrate, forming assumed intermediate $VO_2@M_xV_2O_5$(Figure S3b, S4b). The nanorods are broken into nanoparticles (Figure S3a, S4a) in the meantime because of the mechanical effect. The chemical reaction process occurs mostly on the surface due to the nature of the highly viscous mixture. These intermediate $VO_2@M_xV_2O_5$ composites with residual citrates are then undertaken calcination in air to generate core-shell structured $V_2O_5@NaV_6O_{15}$ (Figure 1c) and $V_2O_5@KV_6O_{15}$ NPs (Figure S5a). For $V_2O_5@NaV_6O_{15}$ NPs, there are two series of peaks in the XRD pattern (Figure 1d), which are indexed to V_2O_5 (PDF NO. 00-041-1426, Pmmn space group, orthorhombic)[21, 29-31] and NaV_6O_{15} (PDF NO. 01-077-0146, A2/m space group, monoclinic),[22] respectively, indicating that this compound is composed of orthorhombic V_2O_5 and monoclinic NaV_6O_{15}. The well-defined and intense XRD peaks of $V_2O_5@NaV_6O_{15}$ NPs also reveal a high degree of crystallinity and no obvious impurity is observed. The XRD pattern of $V_2O_5@KV_6O_{15}$ NPs resembles that of $V_2O_5@NaV_6O_{15}$ NPs, also exhibiting a high degree of crystallinity and two series of peaks (Figure S5b) corresponding to V_2O_5 (PDF NO. 00-041-1426, Pmmn space group, orthorhombic)[21, 29-31] and KV_6O_{15} (PDF NO. 01-075-1016, A2/m space group, monoclinic),[23] respectively. The energy dispersive X-ray spectrum (EDS) elemental mapping images show a uniform distribution of K, V and O elements (Figure S6a-d), and the corresponding EDS is displayed in Figure S6e. The as-prepared V_2O_5 NPs are also of orthorhombic phase (Figure S7a, b). Pure NaV_6O_{15} (PDF NO. 01-077-0146, A2/m space group, monoclinic)[22] and pure KV_6O_{15} (PDF NO. 01-075-1016, A2/m space group, monoclinic)[23] NPs have the same morphology as $V_2O_5@MV_6O_{15}$ NPs (Figure S7c-f).

The transmission electron microscope (TEM) (Figure 1e) and high-resolution TEM (HRTEM) (Figure 1f, g) images of as-prepared $V_2O_5@NaV_6O_{15}$ NPs show clearly visible lattice fringes, suggesting a high degree of crystallinity which is

consistent with the results of XRD pattern. Meanwhile, two sets of lattice fringes are found: the outer lattice spacing of about 0.187 nm corresponds to the (11-7) crystal plane of monoclinic NaV_6O_{15}, and the other one of about 0.423 nm corresponds to (001) crystal plane of orthorhombic V_2O_5. The outer layer is ~4.5 nm in width with an obvious interface (red dash line in Figure 1f, g) between the outer and inner crystal phases, which indicates that the as-prepared materials have core-shell heterogeneous structures. The high angle annular dark field (HAADF) images with mapping (Figure 1h-k) indicate the uniform distribution of Na, V and O elements and the corresponding EDS is displayed in Figure S8. All these results from XRD patterns, HRTEM and HAADF images suggest the formation of core-shell heterogeneous $V_2O_5@NaV_6O_{15}$ structures.

3.2 Electrochemical properties of the as-prepared materials

In order to investigate the electrochemical behaviors of the $V_2O_5@NaV_6O_{15}$ NPs as cathode materials, the assembled coin cells are tested by cyclic voltammetry (CV) (Figure 2a). The positions of redox peaks in the first CV curve are marked out in Figure S9. In the first cathodic scan, the peaks situated at 3.61, 3.33, 3.27, 3.08, 2.88 and 2.48 V are observed. Peaks at 3.33 and 3.08 V correspond to Li^+ insertion into V_2O_5 and those at 3.61 (inset of Figure 2a), 3.27, 2.88 and 2.48 V result from Li^+ insertion into NaV_6O_{15}.[20, 21] In the process of anodic scan, peaks at 2.68, 2.97, 3.32, 3.33, 3.48 and 3.63 (inset of Figure 2a) V are observed, which are paired to the peaks located at 2.48, 2.88, 3.08, 3.27, 3.33 and 3.61 V, respectively.[20, 21] In the following cycles, some changes happen to the curves over the voltage range of 2.90-3.60 V in the cathodic processes. The peaks located at 3.27 and 3.08 V shift to 3.25 and 3.13 V, respectively, because of the activation process.[24] The shape and position of other peaks are well maintained. Modified by NaV_6O_{15}, the two pairs of redox peaks at 3.33/3.48 V and 3.13/3.32 V belonging to the backbone V_2O_5 show lower polarization (75 and 95 mV) (Figure 2a), compared to V_2O_5 NPs whose

polarization is ~2 times larger reaching 140 and 175 mV (Figure S10a). It is noted that the second and the third CV curves almost overlap, indicating the excellent reversibility of $V_2O_5@NaV_6O_{15}$ NPs.[21] By contrast, V_2O_5 NPs show a non-negligible decrease in the area of the CV curves (Figure S10a), implying the partly irreversible insertion/extraction of Li^+. Similarly, $V_2O_5@KV_6O_{15}$ NPs are also tested as LIBs cathodes. In the first three CV curves, the similar electrochemical behaviors as $V_2O_5@NaV_6O_{15}$ NPs are observed (Figure S10b). Apparently, modified by KV_6O_{15}, all the three CV curves overlap very well indicating excellent cycling capability and structural stability, probably due to the KV_6O_{15} modification domains acting as a protecting layer. The two pairs of redox peaks of 3.34/3.47 V and 3.14/3.27 V belonging to the backbone V_2O_5 also show lower polarization (both 65 mV) than those of V_2O_5 NPs, which mainly results from the KV_6O_{15} modification domains acting as an ionic and electronic conducting layer.

The assembled batteries with $V_2O_5@NaV_6O_{15}$ and $V_2O_5@KV_6O_{15}$ NPs as cathodes are tested to investigate the electrochemical performances. At a low current density of 200 mA g^{-1}, capacities of 140 and 132 mAh g^{-1} are delivered in the initial discharging process of $V_2O_5@NaV_6O_{15}$ (Figure 2b) and $V_2O_5@KV_6O_{15}$ (Figure S10c) NPs, respectively. After cycling for 200 and 100 times, the capacity retentions are 94.9% and 89.8%, respectively, exhibiting better cycling stability and higher specific capacity than V_2O_5 NPs. In detail, V_2O_5 NPs show a capacity of 95 mAh g^{-1} in the initial discharging process which decreases to 67 mAh g^{-1} after 183 cycles. The corresponding Coulombic efficiency of $V_2O_5@NaV_6O_{15}$ and $V_2O_5@KV_6O_{15}$ NPs show slight fluctuations, while that of V_2O_5 NPs decreases slightly indicating the existence of irreversible Li^+ insertion/extraction (Figure 2b, S10c). At a higher current density of 1000 mA g^{-1}, the discharge capacity of $V_2O_5@NaV_6O_{15}$ NPs increases slowly from 91 to 100 mAh g^{-1} within the first 26 cycles, maintains stable till the 114th cycle, and then shows a slight decrease. After 500 cycles, the capacity drops to 78 mAh g^{-1} with a capacity retention of 85.7%, exhibiting a better cycling capability and higher capacity compared to V_2O_5 NPs which show a second discharge capacity

of 114 mAh g^{-1} and a low capacity retention (Figure 2c). In the rate performance ranging from 100 to 200, 300, 500, 1000, 2000 and back to 100 mA g^{-1}, the average capacities of V$_2$O$_5$@NaV$_6$O$_{15}$ NPs are 149, 137, 128, 120, 109, 85 and 133 mAh g^{-1}, respectively (Figure 2d), and V$_2$O$_5$@KV$_6$O$_{15}$ NPs are 143, 128, 118, 103, 88, 62 and 128 mAh g^{-1}, respectively (Figure S10d). The rate performance of V$_2$O$_5$ NPs is also tested under the same condition and the average capacities only reach 131, 123, 117, 103, 66, 16 and 125 mAh g^{-1}, respectively (Figure 2d). The corresponding discharge/charge curves of V$_2$O$_5$@NaV$_6$O$_{15}$, V$_2$O$_5$@KV$_6$O$_{15}$ and V$_2$O$_5$ NPs are displayed in Figure 2e, 2f and S11, respectively. Under each current density, the corresponding capacities of the former two are much larger than that of the latter one, especially at high current densities, probably due to the enhancement of electronic and ionic conductivity in core-shell heterogeneous structures.

The electrochemical impedance spectra (EIS) in Figure 3a show much lower charge transfer resistance (R$_{ct}$) of pure NaV$_6$O$_{15}$ (135 Ω) and pure KV$_6$O$_{15}$ (214 Ω) NPs than that of V$_2$O$_5$ NPs (430 Ω). After being modified, V$_2$O$_5$@NaV$_6$O$_{15}$ (124 Ω) and V$_2$O$_5$@KV$_6$O$_{15}$ (208 Ω) NPs also showed lower R$_{ct}$ than that of V$_2$O$_5$ NPs, indicating a better electronic migration of core-shell heterogeneous structures.[25] The Li$^+$ diffusivity (D$_{Li}$) was investigated via galvanostatic intermittent titration technique (GITT) (details can be found in Figure S12-13 and Scheme 1 in the Supporting Information).[26] The D$_{Li}$ have been calculated based on our GITT data (Figure S12a-e). The D$_{Li}$ of V$_2$O$_5$@NaV$_6$O$_{15}$, V$_2$O$_5$@KV$_6$O$_{15}$, pure NaV$_6$O$_{15}$, pure KV$_6$O$_{15}$ and bare V$_2$O$_5$ NPs show some of regularity versus the state of discharge (Figure 3b and S12f). The D$_{Li}$ show a decrease by a couple of orders of magnitude while the materials reach discharge state from transition state. The average D$_{Li}$ values of pure NaV$_6$O$_{15}$, pure KV$_6$O$_{15}$ and bare V$_2$O$_5$ NPs are 1.31×10^{-10}, 2.19×10^{-10} and 4.68×10^{-11} cm^2 s^{-1}, respectively, between 3.16 and 3.5 V (Figure S12f). Bare V$_2$O$_5$ NPs show D$_{Li}$ values of 5.39×10^{-13}, 1.01×10^{-12} cm^2 s^{-1} at 3.38 and 3.18 V, respectively. After being modified by NaV$_6$O$_{15}$, the D$_{Li}$ values were lifted to 2.13×10^{-11} and 2.39×10^{-10} cm^2 s^{-1}, respectively. These values are 1.36×10^{-11} and $8.34 \times$

10

10^{-12} cm^2 s^{-1}, respectively in the case of KV$_6$O$_{15}$ modification (Figure 3b). After being modified, the D_{Li} values of V$_2$O$_5$ are improved by 236 times at most and 8 times at least. The pure KV$_6$O$_{15}$ NPs shows a high initial capacity of 176 mA h g^{-1} probably due to its low degree of crystallinity and 82% of that come from the plateaus below 3.0 V. Under higher rate, the capacity contribution from plateaus at ~2.5 V decreases a lot (Figure S1b). The improvement both in electronic and ionic conductivity for V$_2$O$_5$@MV$_6$O$_{15}$ NPs is believed to contribute to the enhancement of their electrochemical performances. The comparison of the electrochemical performances between V$_2$O$_5$@MV$_6$O$_{15}$ NPs and other previously reported results are showed in Table S1. It is easy to note that the V$_2$O$_5$@MV$_6$O$_{15}$ NPs exhibit good cycling stability and high capacity.

As reported previously, core-shell heterostructures can not only provide a protective layer but also produce a synergistic effect during the discharge/charge processes, thus enhancing the overall electrochemical properties.[13-17,27-29] To verify the synergistic mechanism of the heterostructures, we conducted the time-resolved *in-situ* two-dimensional (2D) XRD tests for V$_2$O$_5$@MV$_6$O$_{15}$ and V$_2$O$_5$ NPs. Obviously, the (001) and (101) reflection peaks of V$_2$O$_5$ NPs show an all the way down to lower positions during the initial discharging process (Figure 4a, b). These two peaks show a straight-climb-up tendency to their original positions in the following charging processes. In the second discharging process, the two reflection peaks keep the same shifting mode, during which V$_2$O$_5$ takes an α-ε-δ phase transition with the increase of lattice constant *c* and small vibration of the lattice constants *a* and *b*.[29-31] During successive Li$^+$ insertion/extraction and phase transition processes, the crystal structures may not accommodate fiercely vibration of the lattice and slight lattice collapse probably accumulates, causing deactivation of the active materials, especially under the high rate operation. However, for V$_2$O$_5$@NaV$_6$O$_{15}$ NPs, the discharge curve shows a plateau at 3.37 V and correspondingly, the (001) and (101) reflection peaks shift to lower angle during the discharging processes (Figure 4c, d). At the end of the discharging process, plateau at 3.24 V belonging to NaV$_6$O$_{15}$ appears.

Consequently, the (104) and (30-4) reflection peaks shift to higher and lower angles, respectively. Instead of staying still, the (001) and (101) reflection peaks still shift to lower angle,[29] which means a slower discharge of V_2O_5. Right at the end of this plateau, about 3.17 V, another plateau belonging to V_2O_5 arises. The (001) and (101) reflection peaks continuously shift to lower angle and stay still when the discharging process of V_2O_5 is accomplished. After a cliff-down to lower angle, a plateau at 2.88 V belonging to NaV_6O_{15} arises, and the (104) and (30-4) reflection peaks disappear forming one reflection all through the subsequent discharging process including the plateau at about 2.52 V. In the subsequent charging process, plateaus at 2.68, 2.96, 3.25, 3.29, 3.45, and 3.65 V appear in succession. Compared to V_2O_5 NPs, the plateau at 3.29 V connecting the end and the beginning of the plateaus situated at 3.25 and 3.45 V, makes the former one a weak-ending and the later one a soft-beginning. All the peaks show highly invertible cyclical variation in position, confirming highly reversible Li^+ insertion/extraction.[29,30,32] Therefore, the above results demonstrate that NaV_6O_{15} layer can provide a buffering structure and faster diffusion channel for Li^+, buffering the drastic structural variation and smoothing the Li^+ diffusion for the backbone V_2O_5, consistent with the changing of D_{Li} value versus the state of discharge of $V_2O_5@NaV_6O_{15}$ NPs.[29] For $V_2O_5@KV_6O_{15}$ NPs, same shifting model of reflection peaks are observed during *in-situ* XRD testing processes (Figure 4e, f), suggesting that KV_6O_{15} layer can provide the same synergetic effect in $V_2O_5@KV_6O_{15}$ core-shell heterostructures. What's more, the structurally stable MV_6O_{15} layer of higher electronic conductivity can restrain the exfoliation of V_2O_5 outer layers, thus enhancing the cycling life of V_2O_5.[18, 19] In this regard, the synergistic effect of the core-shell heterostructures plays a great role in enhancing the electrochemical performances of both $V_2O_5@NaV_6O_{15}$ and $V_2O_5@KV_6O_{15}$ NPs.[13,33-35] The morphologies of $V_2O_5@NaV_6O_{15}$, $V_2O_5@KV_6O_{15}$ and V_2O_5 NPs after 500 cycles at the current density of 1A g^{-1} were also demonstrated. Apparently, the first two kept almost unchanged only with small cracks, while the later cracked into smaller particles, indicating that the $V_2O_5@MV_6O_{15}$ core-shell NPs have better

structural stability (Figure S14). A schematic illustration showing the synergistic effect between the two components in the lithiation/delithiation processes was displayed in Figure S15. During the Li^+ insertion/extraction in/from V_2O_5 processes, the outer MV_6O_{15} layers can buffer the strain and restrain the inner V_2O_5 NPs from cracking. Meanwhile, the Li^+ diffusion was accelerated by 8 times at least.

4　Conclusion

In conclusion, through a facile "semi-solid" synthetic method, $V_2O_5@MV_6O_{15}$ (M=Na, K) NPs were successfully constructed. Core-shell heterogeneous $V_2O_5@NaV_6O_{15}$ NPs showing a 4.5 nm-thick NaV_6O_{15} protecting layer were confirmed by TEM. When tested as a cathode in LIBs, the $V_2O_5@NaV_6O_{15}$ NPs showed a pristine discharge capacity of 140 mAh g^{-1} at 200 mA g^{-1}, with a capacity retention of 94.9% after cycling for 200 times. $V_2O_5@KV_6O_{15}$ NPs showed the same improved electrochemical behaviors compared to V_2O_5 NPs during the electrochemical testing processes. The enhanced performances are attributed to the synergistic effects from the outer MV_6O_{15} protecting layers which were confirmed by the *in-situ* XRD testing results. Firstly, the MV_6O_{15} with a stable crystal structure can restrain the exfoliation of V_2O_5 outer layers, thus enhancing the cycling life. Secondly, MV_6O_{15} with higher electronic conductivity and faster ionic diffusion path can reduce the R_{ct} value and enhance the Li^+ diffusion. Thirdly and importantly, MV_6O_{15} layers showed a synergistic effect, i.e. buffering and smoothing the Li^+ diffusion during the lithium-ion insertion/extraction processes. This work presents an efficient way to construct core-shell heterogeneous structures with a synergistic effect and this strategy could be widely applied to enhance the electrochemical performance of electrode materials.

References

[1] J. B. Goodenough; K. S. Park, The Li-ion rechargeable battery: a perspective. J. Am. Chem. Soc. 135 (2013) 1167-1176.

[2] W. Waag, C. Fleischer, D. U. Sauer, Critical review of the methods for monitoring of lithium-ion batteries in electric and hybrid vehicles. J. Power Sources 258 (2014) 321-339.

[3] G. Zhou, F. Li, H. M. Cheng, Progress in flexible lithium batteries and future prospects. Energy Environ. Sci. 7 (2014) 1307-1338.

[4] L. Lu, X. Han, J. Li, J. Hua, M. Ouyang, A review on the key issues for lithium-ion battery management in electric vehicles. J. Power Sources 226 (2013) 272-288.

[5] Q. Pang, X. Liang, C. Y. Kwok, L. F. Nazar, Advances in lithium–sulfur batteries based on multifunctional cathodes and electrolytes. Nat. Energy 1 (2016) 16132.

[6] F. Lin, D. Nordlund, Y. Li, M. K. Quan, L. Cheng, T. C. Weng, Y. Liu, H. L. Xin, M. M. Doeff, Metal segregation in hierarchically structured cathode materials for high-energy lithium batteries. Nat. Energy 1 (2016) 15004.

[7] X. Fan, Y. Zhu, C. Luo, L. Suo, Y. Lin, T. Xu, K. Gao, Pomegranate-structured conversion-reaction cathode with a built-in Li source for high-energy Li-ion batteries. ACS Nano 10 (2016) 5567-5577.

[8] R. P. Qing, J. L. Shi, D. D. Xiao, X. D. Zhang, Y. X. Yin, Y. B. Zhai, L. Gu, Y. G. Guo, Enhancing the kinetics of Li-rich cathode materials through the pinning effects of gradient surface Na^+ doping. Adv. Energy Mater. 6 (2016) 1501914.

[9] D. Chao, X. Xia, J. Liu, Z. Fan, C. F. Ng, J. Lin, H. Zhang, Z. X. Shen, H. J. Fan, A V_2O_5/conductive-polymer core/shell nanobelt array on three-dimensional graphite foam: a high-rate, ultrastable, and freestanding cathode for lithium-ion batteries. Adv. Mater. 26 (2014) 5794-5800.

[10] H. B. Wu, A. Pan, H. H. Hng, X. W. Lou, Template−assisted formation of rattle−type V_2O_5 hollow microspheres with enhanced lithium storage properties. Adv. Funct. Mater. 23 (2013) 5669-5674.

[11] Y. Ma, A. Huang, H. Zhou, S. Ji, S. Zhang, R. Li, H. Yao, X. Cao, P. Jin, Template-free formation of various V_2O_5 hierarchical structures as cathode materials for lithium-ion batteries. J. Mater. Chem. A 5 (2017) 6522-6531.

[12] M. Xie, X. Sun, H. Sun, T. Porcelli, S. M. George, Y. Zhou, J. Lian, Stabilizing an amorphous V_2O_5/carbon nanotube paper electrode with conformal TiO_2 coating by atomic layer deposition for lithium ion batteries. J. Mater. Chem. A 4 (2016) 537-544.

[13] Q. Wang, J. Sun, Q. Wang, D. A. Zhang, L. Xing, X. Xue, Electrochemical performance of α-MoO_3–In_2O_3 core–shell nanorods as anode materials for lithium-ion batteries. J. Mater. Chem. A 3 (2015) 5083–5091.

[14] S.Yuan, Y. B. Liu, D. Xu, D. L. Ma, S. Wang, X. H. Yang, Z. Y. Cao, X. B. Zhang, Pure single-crystalline $Na_{1.1}V_3O_{7.9}$ nanobelts as superior cathode materials for rechargeable sodium-ion batteries. Adv. Sci. 2 (2015) 1400018.

[15] Q. Lian, G. Zhou, X. Zeng, C. Wu, Y. Wei, C. Cui, W. Wei, L. Chen, C. Li, Carbon coated SnS/SnO_2 heterostructures Wrapping on CNFs as an improved-performance anode for Li-ion batteries: lithiation-induced structural optimization upon cycling. ACS Appl. Mater. Interfaces 8 (2016) 30256-30263.

[16] E. Lee, J. Lu, Y. Ren, X. Luo, X. Zhang, J. Wen, D. Miller, A. DeWahl, S. Hackney, B. Key, D. Kim, M. D. Slater, C. S. Johnson, Layered P2/O3 intergrowth cathode: toward high power Na-ion batteries. Adv. Energy Mater. 4 (2014) 1400458.

[17] Z. Wu, S. Ji, T. Liu, Y. Duan, S. Xiao, Y. Lin, K. Xu, F. Pan, Aligned Li^+ tunnels in core–shell $Li(Ni_xMn_yCo_z)O_2$@$LiFePO_4$ enhances its high voltage cycling stability as Li-ion battery cathode. Nano Lett. 16 (2016) 6357-6363.

[18] Y. Zhao, C. Han, J. Yang, J. Su, X. Xu, S. Li, L. Xu, R. Fang, H. Jiang, X. Zou, B. Song, L. Mai, Q. Zhang, Stable alkali metal ion intercalation compounds as optimized metal oxide nanowire cathodes for lithium batteries. Nano Lett. 15 (2015) 2180-2185.

[19] J. Meng, Z. Liu, C. Niu, X. Xu, X. Liu, G. Zhang, X. Wang, M. Huang, Y. Yu, L. Mai, A synergistic effect between layer surface configurations and K ions of potassium vanadate nanowires for enhanced energy storage performance. J. Mater.

Chem. A 4 (2016) 4893-4899.

[20] J. K. Kim, B. Senthilkumar, S. H. Sahgong, J. H. Kim, M. Chi, Y. Kim, New chemical route for the synthesis of β-Na$_{0.33}$V$_2$O$_5$ and its fully reversible Li intercalation. ACS Appl. Mater. Interfaces 7 (2015) 7025-7032.

[21] H. Song, C. Zhang, Y. Liu, C. Liu, X. Nan, G. Cao, Facile synthesis of mesoporous V$_2$O$_5$ nanosheets with superior rate capability and excellent cycling stability for lithium ion batteries. J. Power Sources 294 (2015) 1-7.

[22] S. Kubuki, K. Matsuda, K. Akiyama, T. Nishida, [57]Fe-Mössbauer study of electrically conductive alkaline iron vanadate glasses. J. Radioanal. Nucl. Chem. 299 (2014) 453-459.

[23] R. P. Ozerov, G. A. Golder, G. S. Zhdanov, X-ray diffraction study of M$_{0.33}$V$_2$O$_5$ (M= Na, K) vanadium bronzes. Kristallografiya 2 (1957) 217-225.

[24] M. M. Rahman, A. Z. Sadek, I. Sultana, M. Srikanth, X. J. Dai, M. R. Field, D. G. McCulloch, S. B. Ponraj, Y. Chen, Self-assembled V$_2$O$_5$ interconnected microspheres produced in a fish-water electrolyte medium as a high-performance lithium-ion-battery cathode. Nano Res. 8 (2015) 3591-3603.

[25] Q. Wang, B. Yu, X. Li, L. Xing, X. Xue, Core–shell Co$_3$O$_4$/ZnCo$_2$O$_4$ coconut-like hollow spheres with extremely high performance as anode materials for lithium-ion batteries. J. Mater. Chem. A 4 (2016) 425-433.

[26] W. Weppner, R. A. Huggins, Determination of the kinetic parameters of mixed-conducting electrodes and application to the system Li$_3$Sb. J. Electrochem. Soc. 124 (1977) 1569−1578.

[27] H. Wang, D. Ma, X. Huan, Y. Huang, X. Zhang, General and controllable synthesis strategy of metal oxide/TiO$_2$ hierarchical heterostructures with improved lithium-ion battery performance. Sci. Rep. 2 (2012) 701.

[28] D. A. Zhang, Q. Wang, Q. Wang, J. Sun, L. L. Xing, X. Y. Xue, High capacity and cyclability of hierarchical MoS$_2$/SnO$_2$ nanocomposites as the cathode of lithium-sulfur battery. Electrochim. Acta 173 (2015) 476-482.

[29] C. Niu, X. Liu, J. Meng, L. Xu, M. Yan, X. Wang, G. Zhang, Z. Liu, X. Xu, L.

Mai, Three dimensional V_2O_5/NaV_6O_{15} hierarchical heterostructures controlled synthesis and synergistic effect investigated by in situ X-ray diffraction. Nano Energy 27 (2016) 147-156.

[30] Y. Sato, T. Asada, H. Tokugawa, K. Kobayakawa, Observation of structure change due to discharge/charge process of V_2O_5 prepared by ozone oxidation method, using in situ X-ray diffraction technique. J. Power Sources 68 (1997) 674-679.

[31] X. F. Zhang, K. X. Wang, X. Wei, J. S. Chen, Carbon-coated V_2O_5 nanocrystals as high performance cathode material for lithium ion batteries. Chem. Mater. 23 (2011) 5290-5292.

[32] X. Wang, X. Xu, C. Niu, J. Meng, M. Huang, X. Liu, Z. Liu, L. Mai, Earth abundant Fe/Mn-based layered oxide interconnected nanowires for advanced K-ion full batteries. Nano Lett. 17 (2016) 544-550.

[33] W. Zhou, D. Kong, X. Jia, C. Ding, C. Cheng, G. Wen, $NiCo_2O_4$ nanosheet supported hierarchical core–shell arrays for high-performance supercapacitors. J. Mater. Chem. A 2 (2014) 6310-6315.

[34] K. Wang, C. Zhao, S. Min, X. Qian, Facile synthesis of $Cu_2O/RGO/Ni(OH)_2$ nanocomposite and its double synergistic effect on supercapacitor performance. Electrochem. Acta 165 (2015) 314-322.

[35] T. Chen, Y. Tang, W. Guo, Y. Qiao, S. Yua, S. Mu, L. Wang, Y. Zhao, F. Gao, Synergistic effect of cobalt and nickel on the superior electrochemical performances of rGO anchored nickel cobalt binary sulfides." Electrochem. Acta 212 (2016) 294-302.

[36] C. Niu, J. Meng, C. Han, K. Zhao, M. Yan, L. Mai, VO_2 nanowires assembled into hollow microspheres for high-rate and long-life lithium batteries. Nano Lett. 14 (2014) 2873-2878.
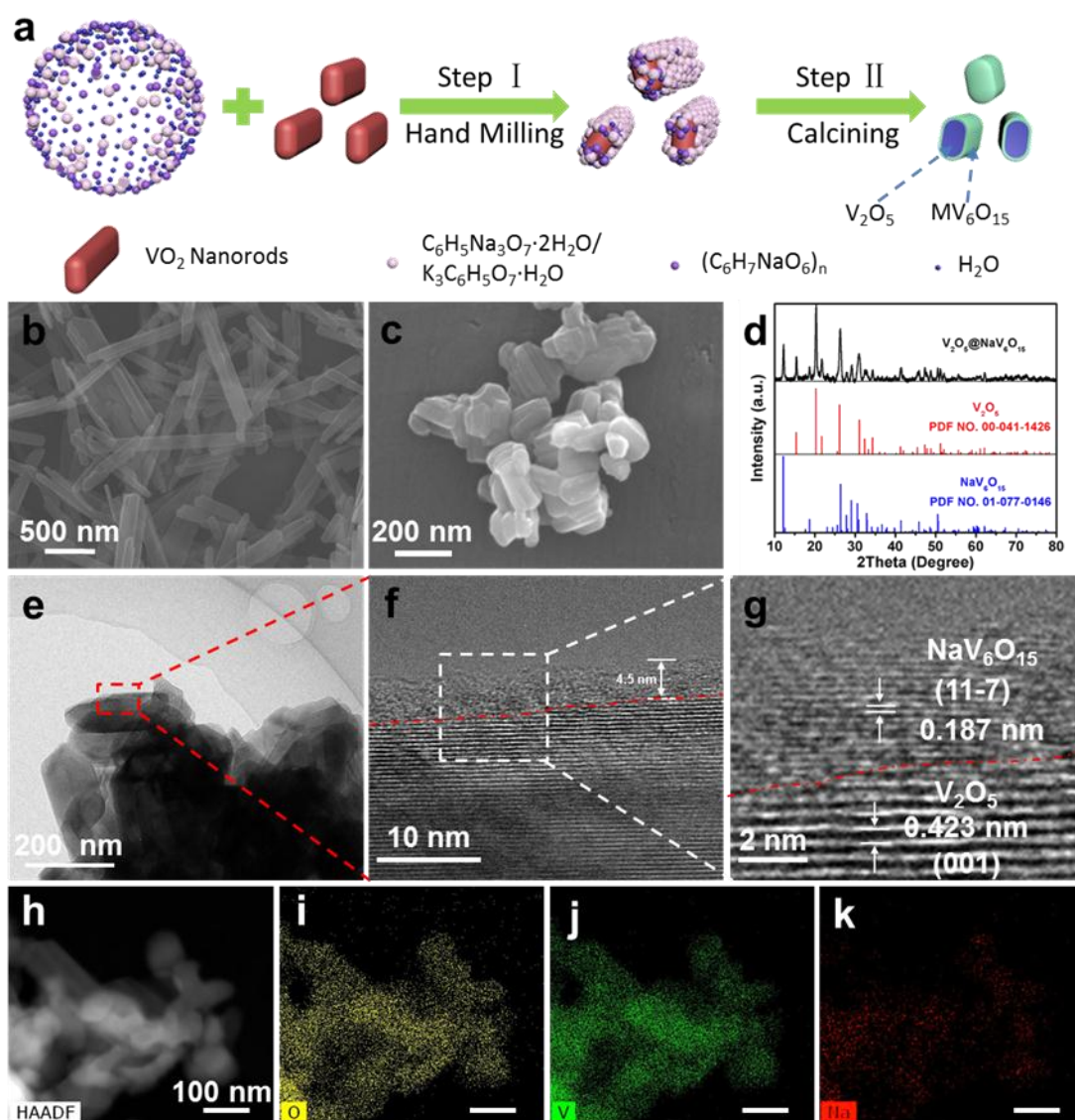
Figure 1. (a) Schematic diagrams of the formation process of core-shell heterogeneous $V_2O_5@MV_6O_{15}$ NPs. SEM images of as-prepared (b) VO_2 nanorods, (c) $V_2O_5@NaV_6O_{15}$ NPs. (d) XRD pattern of $V_2O_5@NaV_6O_{15}$ NPs. (e) TEM and (f, g) HRTEM images of $V_2O_5@NaV_6O_{15}$ NPs. (h-k) HAADF images with mapping of as-prepared $V_2O_5@NaV_6O_{15}$ NPs.
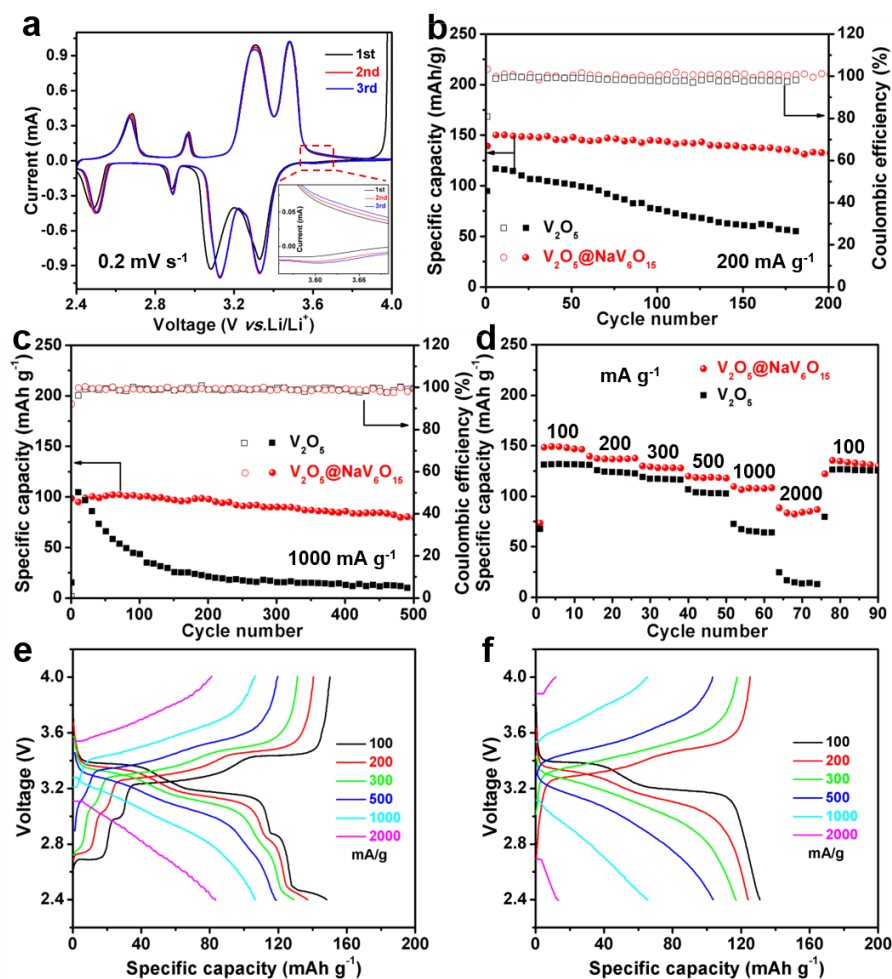
Figure 2. (a) First three CV curves of $V_2O_5@NaV_6O_{15}$ NPs at the scan rate of 0.1 mV s^{-1} of 2.4-4 V. The inset is an enlarged area of the red dashed box. Electrochemical performances of $V_2O_5@NaV_6O_{15}$ NPs (red circles) and V_2O_5 NPs (black squares): cycling performance at (b) 200 mA g^{-1} and (c) 1000 mA g^{-1}; (d) rate performance at different current densities from 100 to 200, 300, 500, 1000 and 2000 mA g^{-1}. The corresponding discharge/charge curves of figure 2d: (e) $V_2O_5@NaV_6O_{15}$ and (f) bare V_2O_5 NPs.
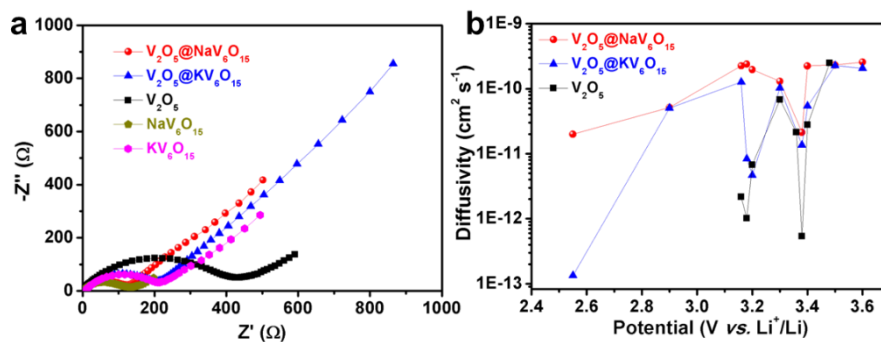
Figure 3. (a) AC impedance plots of $V_2O_5@NaV_6O_{15}$ (red circles), $V_2O_5@KV_6O_{15}$ (blue triangles), bare V_2O_5 nanoparticles (black squares), pure NaV_6O_{15} (dark yellow pentagons) and pure KV_6O_{15} (magenta hexagons). (b) Li^+ diffusivity versus the state of discharge of bare V_2O_5 NPs (black squares), $V_2O_5@NaV_6O_{15}$ (red circles) and $V_2O_5@KV_6O_{15}$ (blue triangles) NPs.
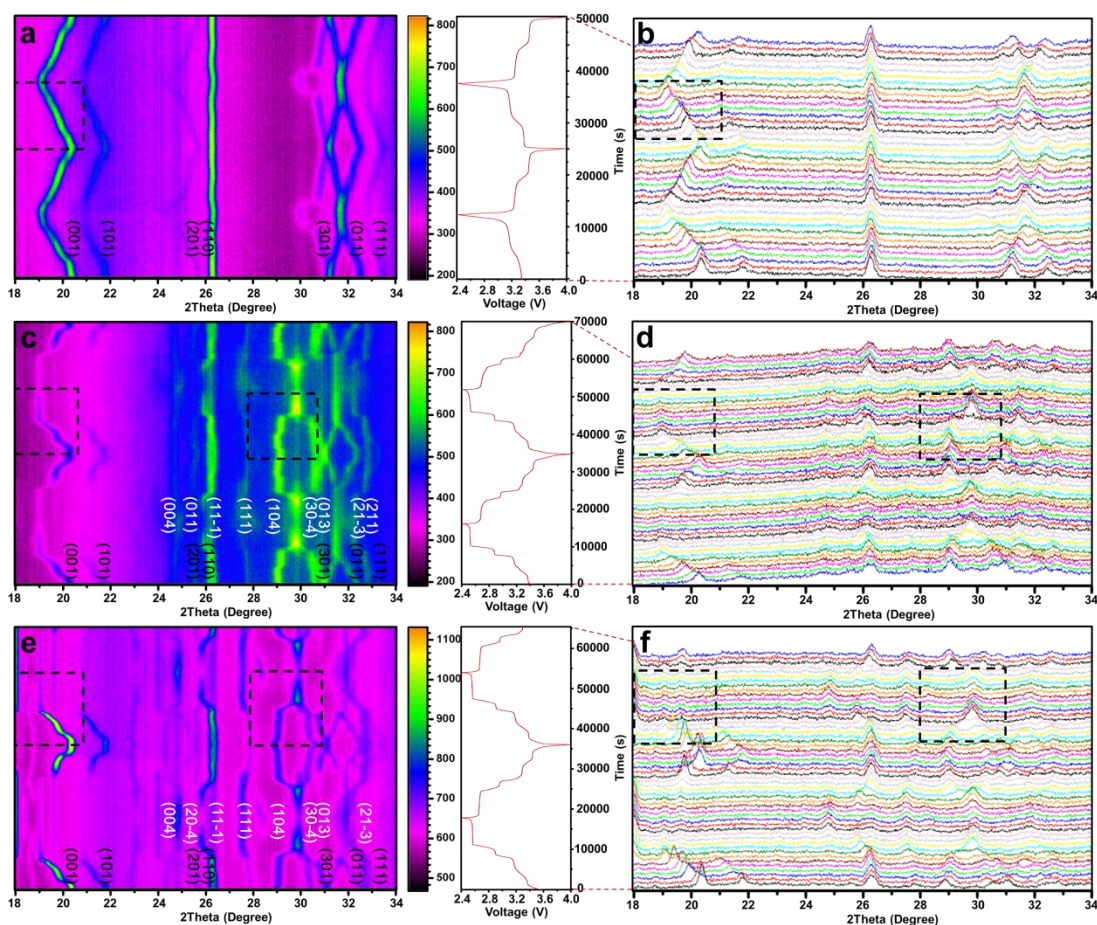
Figure 4. *In-situ* 2D XRD patterns of (a) bare V_2O_5, (c) $V_2O_5@NaV_6O_{15}$ and (e) $V_2O_5@KV_6O_{15}$ NPs, during galvanostatic discharge/charge processes at 40 mA g^{-1}, and (b), (d) and (f) are the corresponding 1D XRD patterns. The horizontal axis represents the selected 2θ regions from 18 to 34°, and time is plotted on the vertical axis. The corresponding voltage curves are plotted in the middle. The diffraction intensity is color coded according to the scale bar on the right of 2D XRD patterns. The reflection peaks in white and black fonts belong to MV_6O_{15} and V_2O_5, respectively, and those weak reflection peaks are omitted.